

# Effect of a marginal inclination on pattern formation in a binary liquid mixture under thermal stress.

F. Croccolo<sup>(1,2)</sup>, F. Scheffold<sup>(1)</sup> and A. Vailati<sup>(3)</sup>

<sup>(1)</sup> *Department of Physics, University of Fribourg, CH-1700 Fribourg, Switzerland*

<sup>(2)</sup> *present address: Laboratoire des Fluides Complexes et leurs Réservoirs - CNRS UMR5150, Université de Pau et des Pays de l'Adour, 64600 Anglet, France and*

<sup>(3)</sup> *Dipartimento di Fisica, Università degli Studi di Milano, I-20133 Milano, Italy*

(Dated: February 19, 2013)

Convective motions in a fluid layer are affected by its orientation with respect to the gravitational field. We investigate the long-term stability of a thermally-stressed layer of a binary liquid mixture and show that pattern formation is strongly affected by marginal inclinations as small as a few milliradians. At small Rayleigh numbers the mass transfer is dominated by the induced large scale shear flow, while at larger Rayleigh numbers it is dominated by solutal convection. At the transition, the balance between the solutal and shear flows gives rise to drifting columnar flows moving in opposite directions along parallel lanes in a Super-Highway configuration. Our findings suggest a potential relevance for the experimental modeling of thermohaline convection in the oceans.

PACS numbers: 47.20.Bp, 47.54.-r, 47.54.-r, 92.10.af

Pattern formation in non-equilibrium systems arises from symmetry breaking of an isotropic initial state [1]. Whenever two symmetry-breaking mechanisms coexist their competition gives rise to a rich phase diagram. A typical example is represented by an inclined layer of liquid under the action of a temperature difference. Tilting the layer can determine a large scale shear flow (LSF). For fairly large inclinations theoretical [2–4] and experimental studies [5–9] reveal rich spatio-temporal dynamics in the phase diagram, characterized by the presence of Busse oscillations, subharmonic oscillations as well as longitudinal and cross rolls. The transitions between different regimes occur at angles of the order of tens of degrees, and pattern formation does not appear to be influenced by small inclination angles of the order of a few degrees or smaller. By adding a second component to the mixture, the compositional stratification also contributes to the convective behavior. A remarkable example is represented by thermohaline circulation in oceans, where both the local salinity and temperature of water contribute to the convective motions, the thickness of the layer of water being modulated by the seafloor [10, 11]. The thermal stress applied to a liquid mixture via a temperature gradient can be quantified by the dimensionless Rayleigh number  $Ra = g\Delta\rho_T h^3/(\eta D_T)$  [12], where  $g$  is the gravity acceleration,  $\Delta\rho_T$  the density difference generated by thermal dilation of the liquid,  $h$  the liquid layer thickness,  $\eta$  its shear viscosity and  $D_T$  the thermal diffusivity. The presence of the thermal stress determines a separating flux of the two components and, in turn, a solutal density difference  $\Delta\rho_c$  throughout the sample, whose value and orientation is quantified by the Soret coefficient  $S_T$  [13, 14]. In the case of a mixture with positive  $S_T$ , as the one used in our study, both  $\Delta\rho_T$  and  $\Delta\rho_c$  contribute to destabilize a sample heated from below.

In this letter we investigate the influence of a small

inclination angle in the range  $0 \text{ mrad} < \alpha < 36 \text{ mrad}$  ( $\alpha < 2^\circ$ ) on the long-term stability of a layer of a binary liquid mixture under thermal stress below the threshold for Rayleigh-Bénard convection ( $Ra_c \simeq 1700$ ). This model system mimicks many of the features of thermohaline circulation. Interestingly, we find the stability of the mixture to be strongly influenced already by small inclination angles, in contrast to the behaviour of simple liquids. The observed convective patterns are arranged into a peculiar Super-Highway configuration, reminiscent of the traffic of vehicles during rush hours. Such pattern differs dramatically from the square, roll, and cross-roll patterns previously reported experimentally [15, 16] and theoretically [17, 18] for binary liquid mixtures heated from below in the absence of inclination.

The binary mixture selected for this study is isobutylbenzene/n-dodecane at 50% weight fraction. The choice of this mixture is motivated by the availability of an accurate and extensive set of thermophysical properties [19]. The sample is delimited by two  $8 \times 40 \times 40 \text{ mm}^3$  square sapphire windows kept at fixed distance and sealed by a circular Viton O-ring gasket with an inner radius  $R = 13 \text{ mm}$ . The geometry corresponds to a moderately high aspect ratio  $R/h = 10$  of the sample. The sapphire windows are in contact with two annular thermo electric devices connected to two independent proportional-integral-derivative (PID) temperature controllers. The temperature of each sapphire window can be controlled independently with an absolute accuracy of 0.01 K and a relative RMS stability of 0.001 K over 24 hours. The annular Peltier elements have an inner radius of  $r = 6.5 \text{ mm}$  that determines a clear aperture suitable to perform optical measurements. The performances and reliability of the cell have been established during a long series of experiments on devices sharing a similar conceptual design (see [21, 22] and references

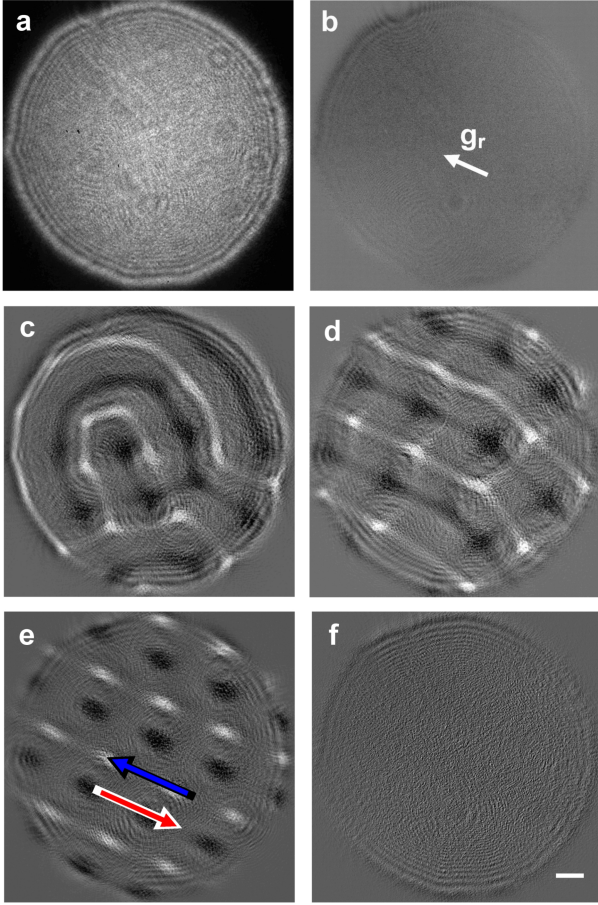


FIG. 1. (color online) Shadowgraph images of the convective patterns:  $Ra = 1320$ ,  $\alpha = 24\text{mrad}$  a, Reference image taken at  $t = 0\text{s}$ . b-f, Difference images; dark zones denote the warmer fluid, which is less concentrated in the denser isobutylbenzene component. Different times shown are: b 150s, c 400s, d 4000s, e 20500s, and f 29000s. The direction of the marginal gravitational acceleration parallel to the cell plane is indicated by an arrow in b. The directions of motion of the lines for the Super-Highway convection are indicated by red and blue arrows in e. The size bar in f corresponds to the sample thickness  $h = 1.3\text{mm}$ .

therein). A  $h = 1.3\text{ mm}$  thick layer of the mixture is hosted inside the thermal gradient cell that can be tilted by using a calibrated screw. We estimate that in the horizontal configuration the accuracy of the tilt angle is better than  $2\text{ mrad}$ . The diagnostic method of choice is a shadowgraph, a visualization technique widely employed in fluid dynamics [23–25]. Its implementation comprises a super-luminous diode (Superlum, Broad Lighter S680) with a wavelength of  $\lambda = (683 \pm 9)\text{ nm}$ , coupled to a single mode optical fiber as a light source. The diverging beam out of the fiber is collimated by using an achromatic doublet lens of focal length  $f = 150\text{ mm}$  positioned at the focal distance from the lens. No other lens is used after the sample cell. A Charged Coupled Device sensor (Vosskühler, CCD4000) with a resolution of

$2048 \times 2048$  pixels of  $7.4 \times 7.4\text{ }\mu\text{m}^2$  is placed at a distance of  $z = (260 \pm 10)\text{ mm}$  from the detector [22].

A typical measurement sequence involves the rapid imposition of a temperature difference by heating from below. As a result, a nearly linear temperature profile is established across the sample in a time  $\tau_T = h^2/D_T \cong 20\text{ s}$ . During the process, we grab continuously shadowgraph images of the convective patterns. The frame rate is set to  $1\text{Hz}$  during the initial fast kinetics and reduced to  $1/60\text{Hz}$  for the subsequent slower phase. A sampling from a typical image sequence corresponding to an inclination of  $24\text{ mrad}$  and to a Rayleigh number  $Ra = 1320$  ( $\Delta T = 8.5\text{ K}$ ) is shown in Fig. 1 (see also Supplementary Movie S1). A reference background image is taken before applying the temperature gradient to the fluid mixture (Fig. 1a). This image is then subtracted to all the images subsequently collected at generic time  $t$ . The imposition of the temperature difference is followed by a latency time where no pattern formation occurs (Fig. 1b). This featureless phase ends with the appearance of convective rolls (Fig. 1c). After a few thousands seconds the rolls rearrange towards a more ordered quasi-squared pattern (Fig.1d), a configuration typical of solutal convection in binary mixtures with positive Soret coefficient heated from below [15–17].

Quite surprisingly, after a time of the order of  $10^4\text{s}$  the square patterns start to drift and evolve gradually into sequences of columns of liquid moving in opposite directions along parallel lanes arranged in a Super-Highway configuration (SH) (Fig. 1e). Eventually, the SH patterns might fade away and the convective pattern can become almost featureless (Fig. 1f). At Rayleigh numbers of the order of  $Ra_{SH} \approx 1400$  ( $\Delta T = 9\text{ K}$ ) the SH patterns become stable (Supplementary movie S2). At larger Rayleigh numbers, the patterns display marked oscillations between a drifting square pattern (DS) and an SH one. The long time behavior of the patterns is strongly affected by the marginal inclination angle and by the Rayleigh number (Fig. 2). The phase diagram displays a stable Large Scale Flow (LSF) region at small Rayleigh numbers, where convective patterns are destroyed by the long-term effect of the inclination. At higher Rayleigh numbers the columnar convection is more efficient than the LSF. Under these conditions stable drifting square patterns are present. The intermediate region is characterized by patterns where the competition between LSF and solutal convection becomes apparent and the system displays marked oscillations between drifting square patterns and longitudinal rolls or SH patterns. In a narrow region of the phase space (red stars in Fig.2) the balance between LSF and solutal convection gives rise to a stable SH convection state in which the columns organize into parallel lanes drifting in opposite directions (Fig.1e and Supplementary Movie S3). The white spots, which represent descending columns of colder liquid crossing the cell perpendicularly to the plane of the figure, align into

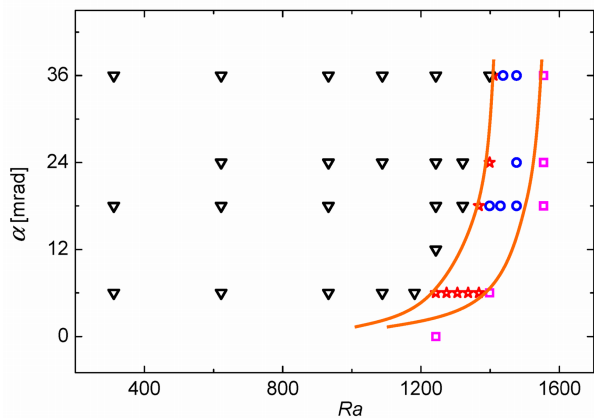


FIG. 2. (color online) Phase diagram of long-term convective behavior: phase diagram of the convective pattern as a function of the Rayleigh number and the inclination angle. Symbols represent the different long-term convective states: ( $\nabla$ ) for Large Scale Flow (LSF); ( $*$ ) for Super-Highway (SH) convection; ( $\circ$ ) for oscillations; ( $\square$ ) for drifting square patterns (DS). The two lines mark the approximate boundaries of the transition region.

parallel lines and move in the direction of the residual gravitational forces  $g_r$  parallel to cell surface, while the dark spots align into another set of lines and move in the opposite direction. The two sets of lines are staggered across the cell plane.

In order to perform a systematic investigation of the evolution of the convective patterns we determined from each image sequence the time evolution of the contrast  $C(t)$  of the images. The image contrast is defined as  $C(t) = \langle [i(t) - i(t)_o]^2 \rangle_{\bar{x}}$  where  $\langle \dots \rangle_{\bar{x}}$  represents the average over the pixels of an image,  $i(t) = I(t) / \langle I(t) \rangle_{\bar{x}}$  is an image normalized by its spatial average, and  $i(t_o)$  is a normalized background image at time  $t_o$  before applying the temperature gradient. The contrast provides a quantitative estimate of the strength of the temperature and concentration modulations generated by the convective motions. Under all the explored experimental conditions, after the imposition of the temperature difference the contrast remains constant for a latency time  $t^*$  lasting from tens to hundreds of seconds (Fig. 3). The latency period is then followed by a rapid growth of the contrast, and by relaxation oscillations leading to a value that remains fairly stable for a second latency time  $t_{LSF}$  related to the inclination of the cell.

Interestingly, up to the time  $t_{LSF}$  the evolution of the contrast under different experimental conditions is qualitatively similar. After that time patterns becomes strongly affected by the Large Scale Flow that determines a dramatic differentiation of the contrast. At  $Ra = 1320$  the drop of the contrast marks the appearance of almost featureless patterns associated to the LSF (black line in Fig. 3). The fact that the contrast does not drop back to its original value is the signature of the presence of

barely detectable fluctuations induced by the shear motion. At  $Ra = 1400$  the balance between LSF and solutal convection gives rise to a SH convective regime (red line in Fig. 3) with a stable contrast, accompanied by small number fluctuations determined by the entrance and exit of the columnar structures into the field of view. At  $Ra = 1480$  the competition between LSF and solutal convection gives rise to the transition between different patterns and the contrast exhibits pronounced oscillations (blue line in Fig. 3). Finally, at  $Ra = 1550$  solutal convection gives rise to square patterns, but the influence of the LSF still determines a drifting of the patterns that gives rise to small number fluctuations (magenta line in Fig. 3).

The presence of relaxation oscillations is a signature that the onset of convection is determined by the destabilization of concentration boundary layers (BLs). Basically, the BLs grow uniformly by diffusion until they reach a critical thickness  $\delta^*$  beyond which convection sets in. An estimate of the critical thickness of the boundary layers can be obtained from the critical dimensionless latency time  $\tau^* = t^* D / h^2$  [26–28], where  $D$  is the diffusion coefficient. Figure 4a-b shows the dimensionless latency time  $\tau^*$  and critical BL thickness  $\delta^*$ , relative to  $h$ , plotted as a function of  $Ra$ . Interestingly, the data in Fig. 4a-b fall onto the same curve independently of the inclination angle. This confirms that the initial stages of pattern formation are not significantly influenced by a marginal inclination of the sample.

After a time  $\tau_{LSF}$  of the order of  $10^4 s$  (Fig. 3) the patterns start to drift, thus marking the start of the influence of the large scale shear flow induced by the inclination of the cell. This time is strongly affected by the inclination angle, as it is apparent from the lack of overlap of the curves for  $\tau_{LSF}(Ra)$  corresponding to different incli-

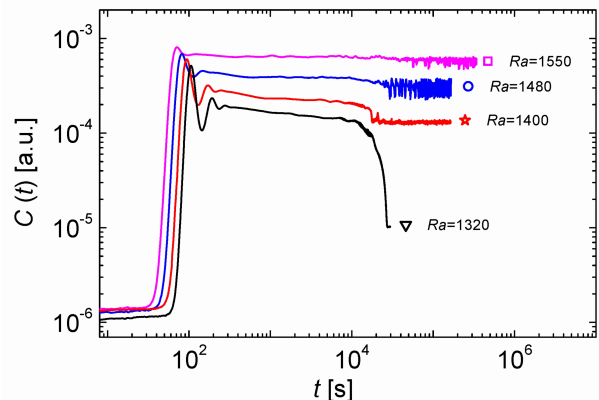


FIG. 3. (color online) Image contrast: contrast of shadow-graph image sequences  $C(t)$  plotted as a function of time. The layer of liquid is tilted at an angle of  $24 mrad$ . The curves correspond to different imposed temperature differences. Continuous lines stand for Rayleigh numbers: (from top to bottom)  $Ra=1550, 1480, 1400, 1320$ .

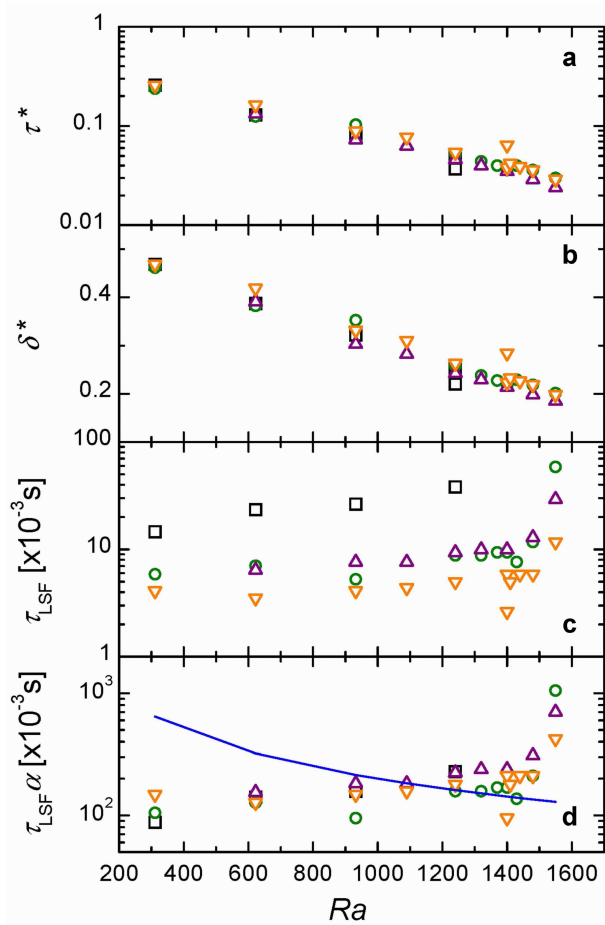


FIG. 4. (color online) Convection parameters: a, Dimensionless critical time  $\tau^*$  for the onset of convection. b, Critical thickness  $\delta^*$  of the dimensionless concentration boundary layer. c, Time for the manifestation of the large-scale shear flow (LSF) related to the inclination,  $\tau_{LSF}$ . d, LSF time multiplied by the inclination angle,  $\tau_{LSF}\alpha$ ; the blue line depicts the  $1/Ra$  behaviour. Different symbols stand for different inclination angles: ( $\square$ ) are for 6 mrad, ( $\triangle$ ) for 18 mrad, ( $\circ$ ) for 24 mrad and ( $\nabla$ ) for 36 mrad.

nation angles (Fig. 4c). A simple understanding of the mechanism behind the influence of the shear flow can be attained by neglecting the effect of convection [2]. The inclination provides a component of the buoyancy force  $F_b \propto g\Delta\rho_T \sin\alpha(1 + \psi)$  aligned parallel to the boundaries, where  $\alpha$  is the inclination angle and  $\psi = \Delta\rho_c/\Delta\rho_T$  is the so-called separation ratio. This force determines a laminar flow of the boundary layers in opposite directions that drives the large-scale flow inside the cell. The buoyancy force is contrasted by the shear force  $F_S \propto \eta\nu$ , where  $\nu \propto 1/\tau_{LSF}$  is the mean velocity of the drifting boundary layers. At steady state the two forces balance each other and, as  $Ra \propto \Delta\rho$ , for small inclination angles  $\tau_{LSF} \propto (Ra)^{-1}$ . This simple relation suggests that the product  $\tau_{LSF}\alpha$  all data should collapse on a single master curve, which is confirmed by our experimental results

as shown in Fig. 4d. Interestingly, the data does not follow the contemplated  $(Ra)^{-1}$  scaling. For large Rayleigh numbers close to the threshold  $Ra_c$  the product shows signs of a divergence. At such large  $Ra$  a slowing down of the shear flow occurs, indicating the dominance of the solutal columnar convective mass transfer over the shear flow.

In the present work we limited our analysis to one liquid mixture with a positive Soret coefficient; it remains an open question whether a similar mechanism can be generally observed in other systems where a temperature and composition stratification coexist. The most interesting case is probably the thermohaline circulation in oceans [10, 11]. Here the cooling determined by wind at the surface of the ocean determines a decrease of the temperature and an increase of the salinity through evaporation, in the presence of a variable landscape at the bottom of the ocean. The combined effect of these factors leads to the large-scale thermohaline circulation, a phenomenon that is still not understood well, due to the simultaneous presence of other effects that contribute to the oceanic currents. Our experimental model system allows to isolate and study independently the fundamental mechanism driving the thermohaline circulation process. This will facilitate progress towards a fundamental understanding of the interplay between large scale flow and local columnar flows.

We thank Henri Bataller for critical reading of the manuscript. F.C. acknowledges financial support from the European Union under FP7 PEOPLE Marie Curie Intra European Fellowship, Contract No. IEF-251131, DyNeFI Project. This project has been financially supported by the Swiss National Science Foundation (Project Nr. 132736).

Correspondence and requests for materials should be addressed to F.C. (fabrizio.croccolo@univ-pau.fr)

- 
- [1] M. C. Cross, and P. C. Hohenberg, *Rev. Mod. Phys.* **65**, 851 (1993).
  - [2] R. M. Clever, and F. H. Busse, *J. Fluid. Mech.* **81**, 107 (1977).
  - [3] F. H. Busse, and R. M. Clever, *J. Eng. Math.* **26**, 1 (1992).
  - [4] F. H. Busse, and R. M. Clever, *Phys. Fluids* **12**, 2137 (2000).
  - [5] K. E. Daniels, B. B. Plapp, and E. Bodenschatz, *Phys. Rev. Lett.* **84**, 5320 (2000).
  - [6] K. E. Daniels, and E. Bodenschatz, *Phys. Rev. Lett.* **88**, 034501(4) (2002).
  - [7] G. Seiden, S. Weiss, J. H. McCoy, W. Pesch, and E. Bodenschatz, *Phys. Rev. Lett.* **101**, 214503(4) (2008).
  - [8] S. Weiss, G. Seiden, and E. Bodenschatz, *New J. Phys.* **14**, 053010(10) (2012).
  - [9] A. Zebib, and M. M. Bou-Ali, *Phys. Rev. E* **79**, 056305 (2009).

- [10] C. Wunsch, Science **298**, 1179 (2002).
- [11] S. Rahmstorf, Nature **42**, 699 (2003).
- [12] T. E. Faber, *Fluid dynamics for physicists* (Cambridge University, Cambridge UK, 1995).
- [13] C. Soret, Arch. Sci. Phys. Nat. **3**, 48 (1879).
- [14] S. R. de Groot and P. Mazur, *Nonequilibrium thermodynamics* (North-Holland, Amsterdam, 1962).
- [15] P. Le Gal, and A. Pocheau, and V. Croquette, Phys. Rev. Lett. **54**, 2501 (1985).
- [16] E. Moses, and V. Steinberg, Phys. Rev. Lett. **57**, 2018 (1986).
- [17] Ch. Jung, and B. Huke, and M. Lücke, Phys. Rev. Lett. **81**, 3651 (1998).
- [18] S. Weggler, and B. Huke, and M. Lücke, Phys. Rev. E **81**, 016309(8) (2010).
- [19]  $D = 9.5 \times 10^{-10} \text{ m}^2 \text{ s}^{-1}$ ,  $S_T = 3.9 \times 10^{-3} \text{ K}^{-1}$ ,  $dn/dT = -4.5 \times 10^{-4} \text{ K}^{-1}$ ,  $dn/dc = 6.3 \times 10^{-2}$ ,  $\alpha = 9.9 \times 10^{-5} \text{ K}^{-1}$ ,  $\beta = 0.13$ ,  $\rho = 79.25 \times 10^{-2} \text{ g cm}^{-3}$ ,  $\eta = 1.1 \times 10^{-2}$  P from [20] and references therein.
- [20] J. K. Platten, M. M. Bou-Ali, P. Costesèque, J. F. Dutrieux, W. Köhler, C. Leppla, S. Wiegand, and G. Wittko, Phil. Mag. **83**, 1965 (2003).
- [21] M. Bernardin, and F. Comitani, and A. Vailati, Phys. Rev. E **85**, 066321(2012).
- [22] F. Croccolo, H. Bataller, and F. Scheffold, J. Chem. Phys. **137**, 234202 (2012).
- [23] G. S. Settles, *Schlieren and Shadowgraph Techniques* (Springer, Berlin, 2001).
- [24] S. Trainoff, and D. S. Cannell, Phys. Fluids **14**, 1340 (2002).
- [25] F. Croccolo, and D. Brogioli, App. Opt. **50**, 3419–3427 (2011).
- [26] L. N. Howard, Proc. 11th Congr. on Appl. Mech., 1109 (1966).
- [27] V. Degiorgio, Phys. Rev. Lett. **41**, 1293 (1978).
- [28] R. Cerbino, and S. Mazzoni, and A. Vailati, and M. Giglio, Phys. Rev. Lett. **94**, 064501 (2005).